Josephson Junction-Based Compact Notch Purcell Filters for Superconducting Qubit Readout

Simona Zaccaria and Antonio Gnudi

***Abstract*—High-fidelity qubit readout in circuit quantum electrodynamics (QED) requires suppressing relaxation due to the Purcell effect, typically achieved through the use of Purcell filters. A key limitation of existing Purcell filter implementations is their large footprint. In this work, we propose a compact notch Purcell filter based on a Josephson junction chain embedded in series with the readout resonator. We analytically derive the conditions for operation in the dispersive regime using a lumped-element model, and validate the concept through an example design that is analyzed through both lumped-element and full electromagnetic simulations. The results indicate that the proposed architecture achieves a Purcell decay time exceeding 1 ms, with a dispersive shift and resonator linewidth of approximately 10 MHz, enabling fast, high signal-to-noise ratio readout. As typical of notch filters, also this solution exhibits an inherent parameter sensitivity. Superconducting quantum interference device (SQUIDs) can be used for postfabrication frequency tuning, at the expense of an increase of the number of required control lines.**

***Index Terms*—Josephson arrays, notch filters, superconducting microwave devices.**

I. Introduction

THE implementation of fault-tolerant quantum information processing requires not only high-fidelity quantum gates but also fast and accurate qubit measurement. In circuit quantum electrodynamics, quantum nondemolition measurement is achieved by dispersively coupling a qubit to a readout resonator. In this regime, the qubit state induces a state-dependent shift in the resonator frequency, allowing the qubit state to be inferred probing the resonator response while the qubit is projected onto one of the computational eigenstates. However, coupling a qubit to a readout resonator introduces an unwanted decay channel for the qubit due to the energy leakage through the resonator into the transmission line, a process known as Purcell effect. The Purcell effect is a key limitation to achieving high-fidelity qubit readout. In principle, it can be mitigated by increasing the detuning between the qubit and the resonator or reducing their mutual coupling. However, these strategies also slow down the measurement process, creating an inherent tradeoff between qubit relaxation and measurement speed. Ideally, one would suppress the Purcell decay without compromising the efficiency or speed of the readout [1].

A common strategy to mitigate this issue is the use of Purcell filters, which can be implemented in various ways. The most common approaches involve introducing a bandpass filter with center frequency tuned to the readout frequency [2] or a notch filter with notch frequency tuned to the qubit frequency [3]. Notch solutions in general require a filter for each qubit. Therefore, in view of a large-scale integration, it is important to design filters with small area occupation. It is also possible to implement broadband filters suitable for multiplexed readout schemes [4]. Another approach consists in exploiting the intrinsic filtering properties of the circuit, such as the distributed nature of the readout resonator and feedline [5].

The architecture we propose is inspired by [6], where it was suggested that a notch Purcell filter can simply be obtained by adding either a capacitor or an inductor in series with the readout resonator. However, the analysis in [6] shows that in the former solution a large capacitance value is required, while the inductor-based approach was not analyzed in depth, probably because incorporating coils into the circuit would significantly increase the area, making such solution less scalable.

Elaborating on the latter concept, our idea is to use an array of Josephson junctions (JJ) to implement a quasi-linear inductor. This quasi-linear inductor has the advantage of occupying minimal space. In order to test this concept, we analyze in detail an example design. Starting from a lumped-element model of the circuit, we analytically derive the conditions for operation in the dispersive regime. We then discuss the simulation results obtained both with a lumped-element and an electromagnetic distributed model and show the extracted key parameters, such as Purcell decay time, dispersive shift, and coupling rate between readout resonator and feedline. The results are promising: a Purcell decay time of the order of milliseconds can be achieved together with a dispersive shift and a coupling rate around 10 MHz, enabling fast readout with high signal-to-noise ratio (SNR). Moreover, in the proposed solution the typical drawback of notch filter architectures, that is the high sensitivity to circuit parameter variations, can be partially mitigated by replacing the junctions with superconducting

Received 3 June 2025; revised 15 July 2025, 4 August 2025, and 1 September 2025; accepted 11 September 2025. Date of publication 15 September 2025; date of current version 30 September 2025. This work was supported in part by QUART&T, a project funded by the Italian Institute of Nuclear Physics (INFN) within the Technological and Interdisciplinary Research Commission (CSN5) and in part by Theoretical Physics Commission (CSN4). *(Corresponding author: Simona Zaccaria.)*

The authors are with the Department of Electrical, Electronic and Information Engineering "Guglielmo Marconi", University of Bologna, 40136 Bologna, Italy, also with the ARCES - Advanced Research Center on Electronic System, University of Bologna, 40125 Bologna, Italy, and also with the INFN, 40127 Bologna, Italy (e-mail: simona.zaccaria4@unibo.it).

Color versions of one or more figures in this article are available at https://doi.org/10.1109/TASC.2025.3610252.

Digital Object Identifier 10.1109/TASC.2025.3610252

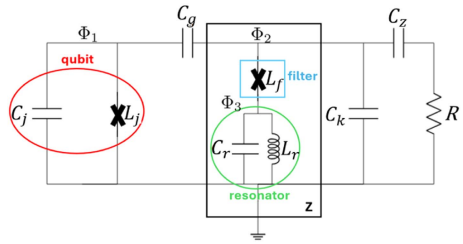

Fig. 1. Lumped-element view of the proposed circuit, consisting in qubit (red), readout resonator (green) and filter inductance (blue). The resistance R accounts for the readout transmission line and the capacitance C_k for the parasitics to ground. The rectangle identifies the impedance Z that must become zero at the qubit frequency to implement the notch filter action.

quantum interference device (SQUIDs), thus making the notch filter tunable.

Our solution is compatible with either single qubit or multiplexed readout solutions, such as the one presented in [7].

The rest of this article is organized as follows. In Section II, the proposed architecture is presented together with the conditions for dispersive regime and the discussion of the effects of nonlinearities. Section III is devoted to the analysis of the example design, both with the lumped-element and the distributed model. A discussion about sensitivity is also included. Finally, Section IV concludes this article.

II. Proposed Architecture

The proposed circuit is schematically represented in its lumped-element form in Fig. 1. The qubit, consisting of a JJ with linear inductance L_j in parallel with capacitor C_j, is capacitively coupled through C_g to the impedence Z formed by the series of the readout resonator, modeled as the parallel L_r-C_r, and the JJ chain with total equivalent linear inductance L_f. The impedance Z is in turn coupled through capacitance C_z to the transmission line used for input–output of the readout signal. In the following calculations a transmission line with characteristic impedance of $50\,\Omega$ terminated at both ends by $50\,\Omega$ loads is assumed. Under these conditions R in Fig. 1 is equal to $25\,\Omega$. Capacitance C_k accounts for parasitics to ground originating from the coupling structures between qubit and impedance Z and between impedance Z and the transmission line.

As explained in [6], the notch Purcell filter effect is obtained by imposing the impedance Z calculated at the qubit frequency to be equal to zero. For the circuit in Fig. 1 this results in

$$Z(\omega_\mathrm{q}) = j\omega_\mathrm{q} L_\mathrm{f} + \frac{j\omega_\mathrm{q} L_\mathrm{r}}{1-\omega_\mathrm{q}^2 C_\mathrm{r} L_\mathrm{r}} = 0 \tag{1}$$

from which it is possible to properly size L_f

$$L_\mathrm{f} = -\frac{L_\mathrm{r}}{1-(\omega_\mathrm{q}/\omega_\mathrm{unr})^2} \tag{2}$$

with $\omega_\mathrm{unr} = 1/\sqrt{L_\mathrm{r} C_\mathrm{r}}$. From (2) it is seen that the condition $\omega_\mathrm{unr} < \omega_\mathrm{q}$ must be met. It should be pointed out that ω_unr is not the dressed resonator mode frequency, which is the one relevant in the readout procedure and is defined and calculated in the next sections, but rather the unloaded resonator frequency. The dressed resonator mode frequency will turn out to be higher than the qubit frequency, which is an important condition to be met to avoid degradation of readout accuracy [8].

A. Condition for the Dispersive Regime

In this subsection, starting from the lumped-element Hamiltonian model of the circuit, we derive analytical conditions for operation in dispersive regime and expressions for dispersive shifts. To simplify the analysis, at this stage we set $R = 0$ thus neglecting dissipation. For the moment we also disregard the nonlinearity introduced by the JJ implementing inductance L_f.

By using standard methods [9] [10], the Lagrangian of the circuit can be derived

$$\mathcal{L} = \frac{1}{2}\dot{\mathbf{\Phi}}_\mathrm{n}^\mathrm{T}\mathbf{C}_\mathrm{n}\dot{\mathbf{\Phi}}_\mathrm{n} - \frac{1}{2}\mathbf{\Phi}_\mathrm{n}^\mathrm{T}\mathbf{L}_\mathrm{n}^{-1}\mathbf{\Phi}_\mathrm{n} - \mathcal{E}_\mathrm{j}^\mathrm{nl}(\Phi_1) \tag{3}$$

where $\mathbf{\Phi}_\mathrm{n}^\mathrm{T} = (\Phi_1, \Phi_2, \Phi_3)$ is the array of node fluxes defined in Fig. 1 and $\mathcal{E}_\mathrm{j}^\mathrm{nl}(\Phi_1) = -E_\mathrm{j}[\cos(\Phi_1/\Phi_\mathrm{o}) + (\Phi_1/\Phi_\mathrm{o})^2/2]$ the nonlinear contribution to the inductive energy of the qubit JJ, with Φ_o the reduced flux quantum and $E_\mathrm{j} = \Phi_\mathrm{o}^2/L_\mathrm{j}$ the JJ energy. Besides, $\mathbf{C}_n$ and $\mathbf{L}_\mathrm{n}^{-1}$ are the capacitance and inverse inductance matrices, respectively, given by

$$\mathbf{C}_\mathrm{n} = \begin{bmatrix} C_\mathrm{j}+C_\mathrm{g} & -C_\mathrm{g} & 0 \\ -C_\mathrm{g} & C_\mathrm{g}+C_\mathrm{p} & 0 \\ 0 & 0 & C_\mathrm{r} \end{bmatrix} \tag{4a}$$

$$\mathbf{L}_\mathrm{n}^{-1} = \begin{bmatrix} 1/L_\mathrm{j} & 0 & 0 \\ 0 & 1/L_\mathrm{f} & -1/L_\mathrm{f} \\ 0 & -1/L_\mathrm{f} & 1/L_\mathrm{f}+1/L_\mathrm{r} \end{bmatrix} \tag{4b}$$

with $C_\mathrm{p} = C_\mathrm{z} + C_\mathrm{k}$. It is seen that the inverse inductance matrix includes the linear inductance L_f.

Following the procedure outlined in [11], the transformation matrix $\mathbf{S}_\mathrm{n}$ is defined such that $\mathbf{\Phi} = \mathbf{S}_\mathrm{n}^{-1}\mathbf{\Phi}_\mathrm{n}$, with $\mathbf{\Phi}^\mathrm{T} \equiv (\Phi_\mathrm{j}, \Phi_\mathrm{f}, \Phi_\mathrm{r}) \equiv (\Phi_1, \Phi_2 - \Phi_3, \Phi_3)$. This transformation diagonalizes the inverse inductance matrix, that is $\mathbf{L}^{-1} \equiv \mathbf{S}_\mathrm{n}^T\mathbf{L}_\mathrm{n}^{-1}\mathbf{S}_\mathrm{n} = \mathrm{diag}(1/L_\mathrm{j}, 1/L_\mathrm{f}, 1/L_\mathrm{r})$. Upon introducing also $\mathbf{C} \equiv \mathbf{S}_\mathrm{n}^T\mathbf{C}_\mathrm{n}\mathbf{S}_\mathrm{n}$ and $\mathbf{Q} \equiv (Q_\mathrm{j}, Q_\mathrm{f}, Q_\mathrm{r})^\mathrm{T} \equiv \mathbf{C}\dot{\mathbf{\Phi}}$, the Hamiltonian can be written as

$$H = \frac{1}{2}\mathbf{Q}^\mathrm{T}\mathbf{C}^{-1}\mathbf{Q} + \frac{1}{2}\mathbf{\Phi}^\mathrm{T}\mathbf{L}^{-1}\mathbf{\Phi} + \mathcal{E}_\mathrm{j}^\mathrm{nl}(\Phi_\mathrm{j}). \tag{5}$$

Quantization is obtained by introducing the phase and charge operators

$$\hat{\Phi}_\mathrm{k} = \Phi_\mathrm{k}^\mathrm{zpf}(a_\mathrm{k}^\dagger + a_\mathrm{k}) \tag{6a}$$

$$\hat{Q}_\mathrm{k} = i\,Q_\mathrm{k}^\mathrm{zpf}(a_\mathrm{k}^\dagger - a_\mathrm{k}) \tag{6b}$$

for $\mathrm{k} \in \{\mathrm{j}, \mathrm{f}, \mathrm{r}\}$, where

$$\Phi_\mathrm{k}^\mathrm{zpf} = \sqrt{\frac{\hbar\,(\mathbf{C}^{-1})_{kk}}{2\,\omega_\mathrm{k}}} \tag{7a}$$

$$Q_\mathrm{k}^\mathrm{zpf} = \sqrt{\frac{\hbar\,\omega_\mathrm{k}}{2(\mathbf{C}^{-1})_\mathrm{kk}}} \tag{7b}$$

are the phase and charge zero-point fluctuations, respectively, a_k and $a_\mathrm{k}^\dagger$ the ladder operators obeying the commutator relations $[a_\mathrm{m}, a_\mathrm{n}^\dagger] = \delta_{\mathrm{m\,n}}$, and

$$\omega_\mathrm{k} = \sqrt{(\mathbf{C}^{-1})_\mathrm{kk}(\mathbf{L}^{-1})_\mathrm{kk}}. \tag{8}$$

Truncating the nonlinear contribution of the JJ energy to fourth order, i.e., $\mathcal{E}_\mathrm{j}^\mathrm{nl}(\Phi_\mathrm{j}) \simeq -E_\mathrm{j}\frac{(\Phi_\mathrm{j}/\Phi_\mathrm{o})^4}{24}$, assuming the rotating wave approximation (RWA) and considering only the first two energy levels of the qubit, the quantized Hamiltonian reads

$$\begin{aligned} H = {} & \omega_\mathrm{q}\frac{\sigma_\mathrm{z}}{2} + \omega_\mathrm{f} a_\mathrm{f}^\dagger a_\mathrm{f} + \omega_\mathrm{r} a_\mathrm{r}^\dagger a_\mathrm{r} \\ & + g_\mathrm{qf}(\sigma_+ a_\mathrm{f} + \sigma_- a_\mathrm{f}^\dagger) + g_\mathrm{fr}(a_\mathrm{r}^\dagger a_\mathrm{f} + a_\mathrm{r} a_\mathrm{f}^\dagger) \end{aligned} \tag{9}$$

where

$$\omega_\mathrm{q} = \omega_\mathrm{j} - E_\mathrm{c}/\hbar \tag{10a}$$

$$g_\mathrm{qf} = \frac{1}{2}\sqrt{\frac{\omega_\mathrm{f}\omega_\mathrm{j}}{(\mathbf{C}^{-1})_\mathrm{jj}(\mathbf{C}^{-1})_\mathrm{ff}}}\,(\mathbf{C}^{-1})_\mathrm{jf} \tag{10b}$$

$$g_\mathrm{fr} = \frac{1}{2}\sqrt{\frac{\omega_\mathrm{f}\omega_\mathrm{r}}{(\mathbf{C}^{-1})_\mathrm{rr}(\mathbf{C}^{-1})_\mathrm{ff}}}\,(\mathbf{C}^{-1})_\mathrm{rf} \tag{10c}$$

and $E_\mathrm{c} = e^2(\mathbf{C}^{-1})_\mathrm{jj}/2$ is the qubit charging energy.

It should be noted that Hamiltonian (9) does not contain any direct coupling term between qubit and resonator, which is due to the element $(\mathbf{C}^{-1})_\mathrm{jr}$ being identically zero for the given circuit. Nevertheless, the qubit and the resonator are subject to an interaction mediated by the filter. To make this interaction explicit, it is convenient to apply the Bogoliubov transformation defined by the unitary [12]

$$\boldsymbol{U} = \mathbb{I}_\mathrm{q} \otimes \exp[\Lambda(a_\mathrm{f}^\dagger a_\mathrm{r} - a_\mathrm{f} a_\mathrm{r}^\dagger)] \tag{11}$$

under which the annihilation operators transform as $\boldsymbol{U}^\dagger a_\mathrm{f}\boldsymbol{U} = \cos(\Lambda)a_\mathrm{f} + \sin(\Lambda)a_\mathrm{r}$ and $\boldsymbol{U}^\dagger a_\mathrm{r}\boldsymbol{U} = \cos(\Lambda)a_\mathrm{r} - \sin(\Lambda)a_\mathrm{f}$. With the additional choice $\Lambda = \frac{1}{2}\arctan(2\,g_\mathrm{fr}/(\omega_\mathrm{r} - \omega_\mathrm{f}))$, the transformed Hamiltonian becomes

$$\begin{aligned} H' \equiv \boldsymbol{U}^\dagger H \boldsymbol{U} = {} & \omega_\mathrm{q}\frac{\sigma_\mathrm{z}}{2} + \tilde{\omega}_\mathrm{f} a_\mathrm{f}^\dagger a_\mathrm{f} + \tilde{\omega}_\mathrm{r} a_\mathrm{r}^\dagger a_\mathrm{r} \\ & + g_\mathrm{qf}\cos(\Lambda)(\sigma_+ a_\mathrm{f} + \sigma_- a_\mathrm{f}^\dagger) \\ & + g_\mathrm{qf}\sin(\Lambda)(\sigma_+ a_\mathrm{r} + \sigma_- a_\mathrm{r}^\dagger) \end{aligned} \tag{12}$$

where

$$\tilde{\omega}_\mathrm{f} = \omega_\mathrm{f}\cos^2(\Lambda) + \omega_\mathrm{r}\sin^2(\Lambda) - g_\mathrm{fr}\sin(2\Lambda) \tag{13a}$$

$$\tilde{\omega}_\mathrm{r} = \omega_\mathrm{r}\cos^2(\Lambda) + \omega_\mathrm{f}\sin^2(\Lambda) + g_\mathrm{fr}\sin(2\Lambda). \tag{13b}$$

From (12) it is seen that the frequency detuning between filter and resonator $\Delta_\mathrm{fr} = \omega_\mathrm{r} - \omega_\mathrm{f}$ plays an important role in determining the qubit-resonator interaction through the parameter Λ: a large Δ_fr decreases such interaction.

From (12) the conditions for operation in the dispersive regime can be easily derived

$$g_\mathrm{qf}\cos(\Lambda) \ll \omega_\mathrm{q} - \tilde{\omega}_\mathrm{f} \tag{14a}$$

$$g_\mathrm{qf}\sin(\Lambda) \ll \omega_\mathrm{q} - \tilde{\omega}_\mathrm{r}. \tag{14b}$$

It is also possible to calculate the dispersive shifts χ_qf and χ_qr by performing a Schrieffer–Wolff transformation [13] [14] on H' obtaining

$$\chi_\mathrm{qf} = 2\,\frac{g_\mathrm{qf}^2\cos^2(\Lambda)}{\omega_\mathrm{q} - \tilde{\omega}_\mathrm{f}} \tag{15a}$$

$$\chi_\mathrm{qr} = 2\,\frac{g_\mathrm{qf}^2\sin^2(\Lambda)}{\omega_\mathrm{q} - \tilde{\omega}_\mathrm{r}}. \tag{15b}$$

B. Nonlinear Effects Due to the JJ Implementation of L_f

The chain of JJs used to implement the inductance L_f introduces an unwanted nonlinearity in the resonator, mainly due to the strong coupling between resonator and filter. This is an undesirable effect, which can be mitigated by selecting a proper number N of JJs in the chain. In general to evaluate the effect of nonlinearities it is necessary to compute the cross-Kerr, χ_mn, and anharmonicity, α_m, coefficients of the three modes. This can be done by means of Ansys HFSS [15] full electromagnetic simulations followed by postprocessing with the pyEPR package [16]. However, the presence of a chain of N JJs makes the electromagnetic simulation more difficult, significantly increasing the number of required mesh elements and computational cost. Moreover, the simulations must be repeated for different values of N. We address this issue adopting the following method. We perform just one simulation with only one JJ implementing L_f, in addition to the JJ in the qubit. From the simulation results the energy-participation ratios $p_\mathrm{m,i}$ [16] for mode $\mathrm{m} \in \{\mathrm{f,q,r}\}$ and junction $\mathrm{i} \in \{\mathrm{j,f}\}$ are extracted and successively rescaled to account for the actual number N of JJs in L_f, according to the procedure fully detailed in the Appendix.

Using (25) of the Appendix we obtain

$$\chi_\mathrm{mn} = \frac{\hbar\,\bar{\omega}_\mathrm{m}\bar{\omega}_\mathrm{n}}{4}\left[\frac{p_\mathrm{m,j}p_\mathrm{n,j}}{E_\mathrm{j}} + \frac{p_\mathrm{m,f}p_\mathrm{n,f}}{E_\mathrm{f}N^2}\right] \tag{16a}$$

$$\Delta_\mathrm{m} = \frac{1}{2}\sum_{\mathrm{n}\in\{\mathrm{f,q,r}\}}\chi_\mathrm{mn} \tag{16b}$$

$$\alpha_\mathrm{m} = \frac{\chi_\mathrm{mm}}{2} \tag{16c}$$

where $\bar{\omega}_\mathrm{m}$ are the eigenfrequencies calculated by the electromagnetic solver, Δ_m the effective Lamb shifts, and $E_\mathrm{f} = (\frac{\hbar}{2e})^2\frac{1}{L_\mathrm{f}}$. With the above expressions one can determine the minimum value of N required to make the nonlinearity of the JJ chain negligible. In particular, we seek the condition

$$\alpha_\mathrm{r} n_\mathrm{r} \ll \kappa_\mathrm{r} \tag{17}$$

where n_r is the average number of photons in the resonator during read-out and κ_r the resonator linewidth, which is also computed by the electromagnetic simulator. Condition (17) guarantees that the resonator frequency shift when n_r photons are present in the resonator must be smaller than its bandwidth, in order not to degrade the coupling with the readout line.

III. Analysis of an Example Design

In this section, we present an example design to illustrate the potential of the proposed circuit. In sizing the circuit parameters

TABLE I
COMPONENT VALUES OF THE LUMPED-ELEMENT MODEL-BASED EXAMPLE DESIGN

Component	Value
L_j	6.7 nH
C_j	84 fF
L_r	1.77 nH
C_r	436.4 fF
L_f	6.5 nH
C_k	156.6 fF
C_g	6.67 fF
C_z	33.4 fF

Components are defined in fig. 1

TABLE II
SUMMARY OF THE PERFORMANCE PARAMETERS CALCULATED BY QUCAT FOR THE DESIGN OF TABLE I

Quantity	Value
Qubit mode frequency $\bar{\omega}_\mathrm{q}/2\pi$	6.46 GHz
Qubit anharmonicity α_q	204 MHz
Resonator mode frequency $\bar{\omega}_\mathrm{r}/2\pi$	6.94 GHz
Filter mode frequency $\bar{\omega}_\mathrm{f}/2\pi$	3.68 GHz
Purcell decay time T_p	17 ms
Resonator-feedline coupling κ_r	8 MHz
Qubit-resonator dispersive shift χ_qr	10 MHz

The reported frequencies are the mode frequencies.

we aimed at qubit and resonator frequencies in the 6–7 GHz range and qubit anharmonicity $\alpha_\mathrm{q} \simeq 200$ MHz. We set a target Purcell decay time $T_\mathrm{p} > 1$ ms, i.e., sufficiently larger than typical relaxation times of transmons reported in literature [17], at the same time trying to maximize the qubit-resonator dispersive shift χ_qr and resonator linewidth κ_r while maintaining $\chi_\mathrm{qr} \simeq \kappa_\mathrm{r}$, in order to optimize the readout speed time [12]. We started by sizing the parameters of the lumped-element model of Fig. 1 with L_f implemented as a linear inductance. QuCAT [18], an open-source Python library for quantum circuit analysis, has been used to extract mode frequencies, dispersive shifts and mode linewidths. The conditions for dispersive regime have been verified through (14). In a second phase a circuit layout has been drawn and analyzed through full electromagnetic Ansys HFSS [15] simulations assuming a perfect metal-on-Si technology, using then EPR [16] to extract the key performance parameters. Both designs are discussed in the next subsections.

A. Lumped-Element Design

The component values of the example design are listed in Table I and the corresponding parameters extracted with QuCAT in Table II.

The obtained results look promising: the dispersive shift χ_qr is comparable with the resonator linewidth κ_r and both are sufficiently large to enable fast and high-fidelity readout [1]. At the same time, the Purcell decay time T_p remains high, indicating strong protection against additional qubit relaxation due to the readout process. Importantly, this result is achieved while keeping the qubit in the dispersive regime, as is inferred from conditions (14) being satisfied with

$$\frac{g_\mathrm{qf}\sin(\Lambda)}{|\omega_\mathrm{q}-\tilde{\omega}_\mathrm{r}|} = 0.09 \tag{18a}$$

TABLE III
ENERGY PARTICIPATION RATIOS $P_{\mathrm{m,i}}$ EXTRACTED FROM EPR ANALYSIS FOR EACH MODE m AND JJ i

m \ i	j	f
f	0.0015	0.53
q	0.96	0.0062
r	0.029	0.39

$$\frac{g_\mathrm{qf}\cos(\Lambda)}{|\omega_\mathrm{q}-\tilde{\omega}_\mathrm{f}|} = 0.04. \tag{18b}$$

The validity of the analytical approach of Section II-A is verified also by comparing the dispersive shift calculated with (15b), $\chi_\mathrm{qr} = 15$ MHz, against the value extracted with QuCAT, $\chi_\mathrm{qr} = 10$ MHz (see Table II).

B. Circuit Layout and Simulation Results

An Ansys HFSS view of a possible layout implementing the example design discussed above is shown in Fig. 2(a). The qubit is of Xmon type [19] with 160-μm long and 20-μm wide arms and a 20-μm gap between the arms and the ground plane. A zoomed view of the Xmon and of the coupling claw-type capacitance, also highlighting the locations of JJs used for the qubit and the filter L_f, is shown in Fig. 2(b). Overall, this portion of the layout approximately corresponds to L_j, C_j, and C_g of Table I. The $\lambda/4$ resonator is implemented with a coplanar waveguide (CPW) of 50-Ω characteristic impedance and 5.2 mm length. The readout line is terminated at both ends with a 50 Ω load and is coupled to the rest of the circuit with an interdigitated capacitance (C_z in Table I).

As explained in Section II-B, the circuit was simulated with Ansys HFSS using a single JJ for the filter inductance L_f. A 6.15-nH L_f provides a 5-ms Purcell decay time T_p, obtained from HFSS eigenfrequency calculations. It is possible that an even higher value of T_p can be achieved with a finer tuning of the simulation mesh and of L_f.

The number of junctions N, needed to control the nonlinearity introduced by the filter, along with the resulting dispersive shifts were determined using (16) and (17). The energy participation ratios were calculated by an EPR analysis [16] and are reported in Table III. With $N = 10$ we obtain $\chi_\mathrm{qr} \approx 12$ MHz and $\alpha_r \approx 0.5$ MHz. For the calculated resonator linewidth $\kappa_r \approx 10$ MHz, it is seen that (17) is satisfied with $n_\mathrm{r} \simeq 10$. Such photon number is also compatible with the condition $n_\mathrm{r} \ll n_\mathrm{crit}$, where n_crit is the critical resonator photon number, defined as $n_\mathrm{crit} = \frac{\Delta^2}{4g^2}$ [12] with $\Delta = \omega_\mathrm{q} - \tilde{\omega}_\mathrm{r}$ and $g = g_\mathrm{qf}\sin(\Lambda)$. We estimate $n_\mathrm{crit} \approx 30$.

Table IV summarizes the main results obtained with HFSS and EPR simulations. The positive results obtained with the lumped model are confirmed also for this realistic layout.

C. Sensitivity to Variations of Design Parameters

As is typical for high-Q notch filters, the proposed filter exhibits a very narrow stopband, which leads to a large sensitivity to variations of design parameters from nominal values. This is illustrated in Fig. 3, which shows the Purcell decay time

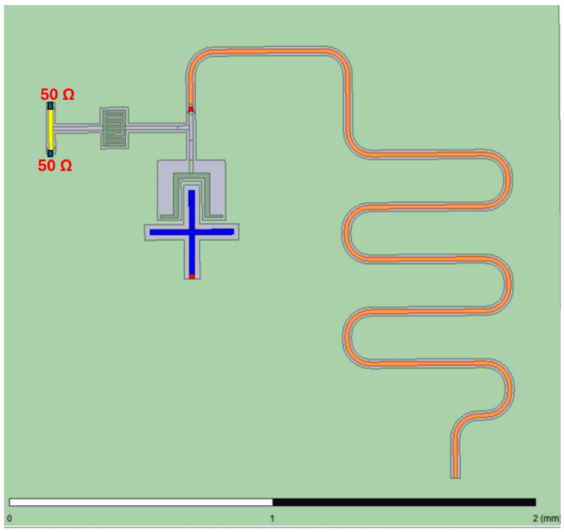

(a)

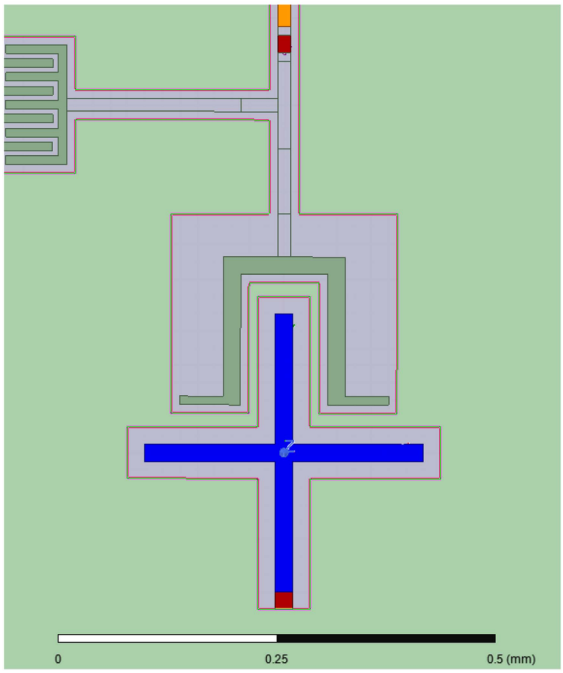

(b)

Fig. 2. (a) Ansys view of the layout of the example design of the proposed circuit, showing the qubit (blue), the $\lambda/4$ CPW readout resonator (orange), the coupling capacitances (green) and a segment of the readout CPW transmission line (yellow). (b) Zoomed-in view of the qubit area, highlighting (red) the locations of the JJs used for the qubit and the filter L_{f}.

estimated through linear circuit analysis with the expression [12]

$$T_{\mathrm{p}} = \frac{C_{\mathrm{j}}}{\mathrm{Re}\{Y_{\mathrm{q}}(\omega_{\mathrm{q}})\}} \tag{19}$$

where Y_{q} is the admittance seen from the qubit, as illustrated in Fig. 4. Both the cases with and without Purcell filter inductance L_{f} are reported in Fig. 3. In the presence of the inductance, T_{p} exhibits a quite narrow peak that ideally should be centered at the nominal qubit frequency. A deviation of more than 0.01 GHz

TABLE IV
SUMMARY OF THE KEY PARAMETERS EXTRACTED WITH ANSYS HFSS SIMULATIONS AND EPR

Parameter	Value
Qubit mode frequency f_{q}	6.45 GHz
Qubit anharmonicity α_{q}	130MHz
Resonator mode frequency f_{r}	6.87 GHz
Filter mode frequency f_{f}	3.66 GHz
Dispersive shift χ_{qr}	12 MHz
Resonator anharmonicity α_{r}	0.5 MHz
Resonator linewidth κ_{r}	10 MHz
Purcell decay time T_{p}	5 ms
Critical photon number n_{crit}	30

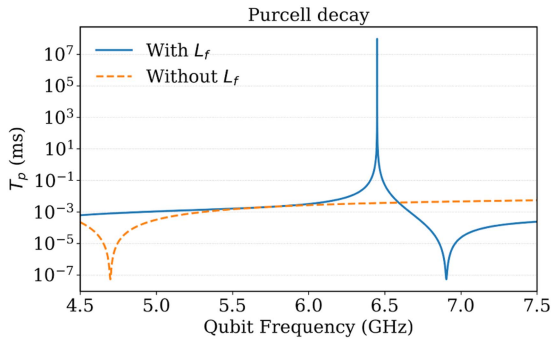

Fig. 3. Purcell decay time computed with (19) with (solid line) and without (dashed line) filtering inductor L_{f}. The peak that appears in the presence of L_{f} should be located at the qubit frequency. The resonator frequency (notch) shifts upward with L_{f} due to the strong coupling between resonator and filter.

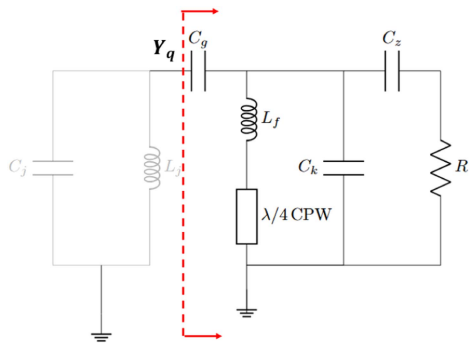

Fig. 4. Definition of the admittance Y_{q} seen from the qubit used for the approximate calculation of T_{p} in (19).

from the nominal frequency causes T_{p} to become less than 1 ms. This implies that small variations in the inductance and capacitance values across the circuit, which cause shifts in qubit or stopband center frequency, can compromise the Purcell protection. This sensitivity problem is common to all notch filter architectures.

The solution to this challenge requires careful postfabrication calibration to align the qubit frequency with the filter notch frequency. This can be achieved by replacing the qubit JJs with SQUIDs, whose effective inductances can be tuned via locally applied magnetic fluxes. The filter design presented here offers an alternative, or an additional, approach by replacing the JJs in the filter itself with SQUIDs [20]. In all cases, such

solutions must be balanced against the increased complexity and cost associated with additional control lines, especially considering that one notch filter per qubit is needed, even in a multiplexed readout architecture. An additional drawback, which is, however, common to all notch filter solutions, is the necessity of maintaining qubit and filter tuned to each other, preventing dynamic qubit frequency tuning. This indicates that the proposed solution is more suitable for 2-qubit gates that use fixed frequency qubits, such as cross-resonance [21] or natively SWAP and iSWAP gates [22].

IV. Conclusion

In this article, a compact notch Purcell filter architecture based on a JJ array implementing a quasi-linear inductance in series with the readout resonator has been presented. Analytical conditions have been derived for operation in the dispersive regime. Simulations of an example design carried out both with a lumped element model and a distributed electromagnetic model show that it is possible to achieve a high Purcell decay time ($T_\mathrm{p} > 1$ ms) as well as a wide resonator bandwidth ($\kappa_\mathrm{r} \approx 10$ MHz) that approximately matches the dispersive shift χ_qr for optimal SNR.

A drawback of the proposed architecture, which is on the other hand typical of all notch filters, is the high sensitivity to parameter variations, essentially due to the quite narrow filter stopband, which makes it easy for the qubit frequency to fall outside the protected band. In the proposed solution, this issue can be mitigated by replacing the JJs with SQUIDs, allowing for in-situ tunability.

We believe the proposed scheme can represent a valid contribution toward the high-level scalability of superconducting circuits for quantum computing applications.

Appendix

Let us consider a superconducting circuit containing M arrays of JJs, N_i being the number of series JJs in the ith array. The potential energy of the ith array can be written as

$$V_\mathrm{i} = -N_\mathrm{i}^2 E_\mathrm{i} \cos(\phi_\mathrm{i}/N_\mathrm{i}) \tag{20}$$

where $E_\mathrm{i} = (\frac{\hbar}{2e})^2 \frac{1}{L_\mathrm{i}}$, L_i being the total linear inductance, and $\phi_\mathrm{i} = \Phi_\mathrm{i}/\Phi_\mathrm{o}$ is the total reduced flux across the entire array.

The nonlinear part of the Hamiltonian reads

$$\begin{aligned} H_\mathrm{NL} &= -\sum_{\mathrm{i}=1}^{M} N_\mathrm{i}^2 E_\mathrm{i}[\cos(\phi_\mathrm{i}/N_\mathrm{i}) + \phi_\mathrm{i}^2/(2N_\mathrm{i}^2)] \\ &\simeq -\sum_{\mathrm{i}=1}^{M} E_\mathrm{i} \frac{\phi_\mathrm{i}^4}{24 N_\mathrm{i}^2} \end{aligned} \tag{21}$$

where the approximation is equivalent to truncating the Taylor expansion to fourth order. As demonstrated in [16], the operator ϕ_i can be expressed as the sum of the reduced mode flux operators as

$$\phi_\mathrm{i} = \sum_\mathrm{m} \phi_{\mathrm{m,i}}(a_\mathrm{m}^\dagger + a_\mathrm{m}) \tag{22}$$

where m is the mode label and $\phi_\mathrm{m,i}$ is the dimensionless, real-valued, quantum zero-point fluctuation of the ith reduced flux in mode m, which can be written in terms of the energy-participation ratio $p_\mathrm{m,i}$ of the ith array in mode m and the linear mode eigenfrequency $\bar{\omega}_\mathrm{m}$ as

$$\phi_\mathrm{m,i}^2 = p_\mathrm{m,i} \frac{\hbar \bar{\omega}_\mathrm{m}}{2E_\mathrm{i}}. \tag{23}$$

By substituting (23) and (22) in (21) and applying the RWA, the nonlinear part of the Hamiltonian becomes

$$\begin{aligned} H_\mathrm{NL} \simeq &-\sum_\mathrm{m} \left[\hbar \Delta_\mathrm{m} \hat{a}_\mathrm{m}^\dagger \hat{a}_\mathrm{m} + \frac{1}{2} \hbar \alpha_\mathrm{m} \hat{a}_\mathrm{m}^{\dagger 2} \hat{a}_\mathrm{m}^2 \right] \\ &- \sum_{\mathrm{n} \neq \mathrm{m}} \frac{1}{2} \hbar \chi_{mn} \hat{a}_\mathrm{m}^\dagger \hat{a}_\mathrm{m} \hat{a}_\mathrm{n}^\dagger \hat{a}_\mathrm{n} \end{aligned} \tag{24}$$

where Δ_m and α_m are the effective Lamb shift and anharmonicity of mode m, respectively, and χ_mn the cross-Kerr frequency shift between modes m and n, given by

$$\begin{aligned} \chi_\mathrm{mn} &= \sum_{\mathrm{i}=1}^{M} \frac{1}{\hbar} \frac{E_\mathrm{i}}{N_\mathrm{i}^2} \phi_{\mathrm{m,i}}^2 \phi_{\mathrm{n,i}}^2 \\ &= \sum_{\mathrm{i}=1}^{M} \frac{\hbar \bar{\omega}_\mathrm{m} \bar{\omega}_\mathrm{n}}{4E_\mathrm{i}} \frac{p_\mathrm{m,i} p_\mathrm{n,i}}{N_\mathrm{i}^2} \end{aligned} \tag{25a}$$

$$\Delta_\mathrm{m} = \frac{1}{2} \sum_\mathrm{n} \chi_\mathrm{mn} \tag{25b}$$

$$\alpha_\mathrm{m} = \frac{\chi_\mathrm{mm}}{2}. \tag{25c}$$

Equation (25a) shows that it is possible to carry out electromagnetic simulations with a single junction for each array to calculate mode frequencies and participation ratios and subsequently determine the various χ_mn parameters by appropriately scaling the $p_\mathrm{m,i}$ coefficients with the actual number of junctions N_i, thus saving computational time.

References

[1] E. A. Sete, J. M. Martinis, and A. N. Korotkov, "Quantum theory of a bandpass Purcell filter for qubit readout," *Phys. Rev. A*, vol. 92, no. 1, Jul. 2015, Art. no. 012325.

[2] E. Jeffrey et al., "Fast accurate state measurement with superconducting qubits," *Phys. Rev. Lett.*, vol. 112, May 2014, Art. no 190504.

[3] M. D. Reed et al., "Fast reset and suppressing spontaneous emission of a superconducting qubit," *Appl. Phys. Lett.*, vol. 96, no. 20, May 2010, Art. no. 203110.

[4] S. H. Park et al., "Characterization of broadband Purcell filters with compact footprint for fast multiplexed superconducting qubit readout," *Appl. Phys. Lett.*, vol. 124, no. 4, Jan. 2024, Art. no. 044003.

[5] P. A. Spring et al., "Fast multiplexed superconducting qubit readout with intrinsic Purcell filtering," 2024, *arXiv:2409.04967*. [Online]. Available: https://arxiv.org/abs/2409.04967

[6] N. T. Bronn, E. Magesan, N. A. Masluk, J. M. Chow, J. M. Gambetta, and M. Steffen, "Reducing spontaneous emission in circuit quantum electrodynamics by a combined readout/filter technique," *IEEE Trans. Appl. Supercond.*, vol. 25, no. 5, Oct. 2015, Art. no. 1700410.

[7] J. Heinsoo et al., "Rapid high-fidelity multiplexed readout of superconducting qubits," *Phys. Rev. Appl.*, vol. 10, no. 3, Sep. 2018, Art. no. 034040.

[8] M. Khezri et al., "Measurement-induced state transitions in a superconducting qubit: Within the rotating-wave approximation," *Phys. Rev. Appl.*, vol. 20, Nov. 2023, Art. no. 054008.

[9] M. H. Devoret, *Quantum Fluctuations in Elect. Circuits, Ed. de Physique*. Amsterdam, The Netherlands: Elsevier, 1997.
[10] A. Ciani, D. P. DiVincenzo, and B. M. Terhal, *Lecture Notes on Quantum Electrical Circuits*. Delft, The Netherlands: TU Delft OPEN Publishing, Feb. 2024.
[11] Z. K. Minev, T. McConkey, M. Takita, A. D. Córcoles, and J. M. Gambetta, "Circuit quantum electrodynamics (cQED) with modular quasi-lumped models," 2021, *arXiv:2103.10344*. [Online]. Available: https://arxiv.org/abs/2103.10344
[12] A. Blais, A. L. Grimsmo, S. M. Girvin, and A. Wallraff, "Circuit quantum electrodynamics," *Rev. Modern Phys.*, vol. 93, no. 2, May 2021, Art. no. 025005.
[13] T. G. Landi, "Eigenoperator approach to Schrieffer–Wolff perturbation theory and dispersive interactions," 2024, *arXiv:2409.10656*. [Online]. Available: https://arxiv.org/abs/2409.10656
[14] S. Bravyi, D. P. DiVincenzo, and D. Loss, "Schrieffer–Wolff transformation for quantum many-body systems," *Ann. Phys.*, vol. 326, no. 10, pp. 2793–2826, Oct. 2011.
[15] "Ansys HFSS — 3D high frequency electromagnetic simulation software," Ansys Inc., Canonsburg, PA, USA, 2025," [Online]. Available: https://www.ansys.com/it-it/products/electronics/ansys-hfss
[16] K. Zlatko et al., "Energy-participation quantization of Josephson circuits," *npj Quantum Inf.*, vol. 7, no. 1, 2021, Art. no 131.
[17] M. Bal et al., "Systematic improvements in transmon qubit coherence enabled by niobium surface encapsulation," *npj Quantum Inf.*, vol. 10, no. 1, Apr. 2024, Art. no. 43.
[18] M. F. Gely and G. A. Steele, "QuCAT: Quantum circuit analyzer tool in Python," *New J. Phys.*, vol. 22, no. 1, Jan. 2020, Art. no. 013025.
[19] R. Barends et al., "Coherent Josephson qubit suitable for scalable quantum integrated circuits," *Phys. Rev. Lett.*, vol. 111, no. 8, Aug. 2013, Art. no. 080502.
[20] M. A. Castellanos-Beltran and K. W. Lehnert, "Widely tunable parametric amplifier based on a superconducting quantum interference device array resonator," *Appl. Phys. Lett.*, vol. 91, no. 8, Aug. 2007, Art. no. 083509.
[21] J. M. Chow et al., "Simple all-microwave entangling gate for fixed-frequency superconducting qubits," *Phys. Rev. Lett.*, vol. 107, no. 8, Aug. 2011, Art. no. 080502.
[22] X. Ken et al., "Native two-qubit gates in fixed-coupling, fixed-frequency transmons beyond cross-resonance interaction," *PRX Quantum*, vol. 5, May 2024, Art. no. 020338.